Particle-scale reversibility in athermal particulate media below jamming

Carl F. Schreck,[1,2] Robert S. Hoy,[3] Mark D. Shattuck,[1,4] and Corey S. O'Hern[1,2,5]

[1]*Department of Mechanical Engineering & Materials Science, Yale University, New Haven, Connecticut 06520-8260, USA*
[2]*Department of Physics, Yale University, New Haven, Connecticut 06520-8120, USA*
[3]*Department of Physics, University of South Florida, Tampa, Florida 33620, USA*
[4]*Benjamin Levich Institute and Physics Department, The City College of the City University of New York, New York, New York 10031, USA*
[5]*Department of Applied Physics, Yale University, New Haven, Connecticut 06520-8120, USA*

(Received 30 January 2013; revised manuscript received 4 November 2013; published 25 November 2013)

We perform numerical simulations of repulsive, frictionless athermal disks in two and three spatial dimensions undergoing cyclic quasistatic simple shear to investigate particle-scale reversible motion. We identify three classes of steady-state dynamics as a function of packing fraction ϕ and maximum strain amplitude per cycle $\gamma_{\max}$. Point-reversible states, where particles do not collide and exactly retrace their intracycle trajectories, occur at low ϕ and $\gamma_{\max}$. Particles in loop-reversible states undergo numerous collisions and execute complex trajectories but return to their initial positions at the end of each cycle. For sufficiently large ϕ and $\gamma_{\max}$, systems display irreversible dynamics with nonzero self-diffusion. Loop-reversible dynamics enables the reliable preparation of configurations with specified structural and mechanical properties over a broad range of ϕ.

DOI: 10.1103/PhysRevE.88.052205 PACS number(s): 45.70.−n, 61.43.−j, 62.20.−x, 63.50.Lm

I. INTRODUCTION

Granular materials, foams, and other athermal particulate media are highly dissipative, and therefore must be driven to induce particle motion. Experimental studies of granular media have shown macroscale reversibility of bulk properties such as the packing fraction during cyclic shear [1] and vibration [2]. In addition, experimental and computational studies of 2D foams have identified reversible and irreversible T1 neighbor switching events of individual bubbles during cyclic shear [3]. Researchers have also shown that motion of individual particles transitions from reversible to irreversible beyond a density-dependent critical strain, which decreases with increasing packing fraction, in cyclically sheared dilute suspensions at low Reynolds number [4,5]. In contrast to fluids at low Reynolds number, where the Navier-Stokes equations are time reversible, Newton's equations of motion for strongly dissipative granular media are not, and thus one might assume that they do not display particle-scale reversibility under cyclic driving. In this paper, we determine whether granular media can undergo completely reversible particle-scale motion due to intergrain collisions when subjected to cyclic loading. This broad question has been addressed in several systems, including dilute suspensions [4,5], amorphous metals [6], and more recently in granular materials [7]. One might expect that highly dissipative systems like granular media would never be reversible. Here we show that, on the contrary, there exist wide parameter regimes where athermal particulate systems are reversible. We address this question by performing numerical simulations of frictionless granular materials in two (2D) and three spatial dimensions (3D) undergoing quasistatic cyclic simple shear over a wide range of packing fractions ϕ and shear strain amplitudes $\gamma_{\max}$.

We identify two classes of grain-scale reversible motion: point and loop. For point-reversible dynamics, particles do not collide during the forward cycle, and thus they exactly retrace their trajectories upon reversal. In contrast, particle collisions occur frequently during loop-reversible dynamics, but the system self-organizes so that particles return to the same positions at the beginning of each cycle. We map out the "dynamical phase diagram" versus ϕ and $\gamma_{\max}$. The system transitions from point- to loop-reversible and then from loop-reversible to irreversible [6,7] dynamics with increasing ϕ and $\gamma_{\max}$. We show that the time evolution toward steady-state point- and loop-reversible behavior can be collapsed onto a universal function with power-law scaling at short and intermediate times and exponential decay at long times. We find qualitatively similar behavior for both 2D and 3D systems. Further, we have identified parameter regimes well-below jamming onset where complex spatiotemporal particle dynamics occurs. In contrast, the jamming literature has focused heavily on the response to shear for solid-like particulate systems near jamming onset. Previous studies have assumed incorrectly that the nonlinear response of unjammed systems below ϕ_J is fundamentally different from that near jamming. This is clearly not true for the onset of loop reversibility since the volume fraction corresponding to this onset, $\phi_L(\gamma_{\max})$, decreases continuously below jamming onset with increasing maximum strain amplitude.

In addition, our findings have the potential to improve processing strategies and give insight into the frequency-dependent rheological properties of granular media and other athermal particulate media over a wide range of packing fraction. In particular, exploiting loop-reversibility should enable the design of athermal particulate systems with tunable structural properties, such as an excess of interparticle contacts over that for thermal systems at the same density.

II. MODEL AND METHODS

We perform numerical studies of N athermal spherical particles undergoing quasistatic, cyclic simple shear at constant ϕ using shear-periodic boundary conditions in square (cubic) cells [8]. Particles interact via the pairwise, purely repulsive linear spring potential

$$V(r_{ij}) = \frac{\epsilon}{2}\left(1 - \frac{r_{ij}}{\sigma_{ij}}\right)^2 \Theta(\sigma_{ij} - r_{ij}), \qquad (1)$$

where r_{ij} is the center-to-center separation between particles i and j, $\Theta(x)$ is the Heaviside step function, $\sigma_{ij} = (\sigma_i + \sigma_j)/2$, and σ_i is the diameter of particle i. We focus on bidisperse particle-size distributions, i.e., 50-50 mixtures by number with diameter ratio $\sigma_l/\sigma_s = 1.4$, to frustrate crystallization during shear [9]. In Appendix A, we consider system sizes from $N = 32$ to 512 to assess finite-size effects for packing fractions below and near the onset of jamming ($\phi_J \sim 0.84$ [10] in 2D and ~ 0.65 in 3D) and find that they are small.

The particles are initially placed randomly in the simulation cell at packing fraction ϕ and then relaxed using conjugate gradient energy minimization [9]. We apply simple shear strain by shifting each particle horizontally,

$$x^i_{n,k+1} = x^i_{n,k} + \Delta\gamma y^i_{n,k}, \tag{2}$$

in increments of $\Delta\gamma = 10^{-3}$, where $x^i_{n,k}$ and $y^i_{n,k}$ are the coordinates of particle i at step k of strain cycle n. This method of applying uniform simple shear strain is similar to that employed in recent experiments on granular materials, where disks rest on a substrate made of slats that can move independently to apply uniform strain [11]. After each strain step, we minimize the total potential energy at fixed shear strain, i.e., $\gamma_k = k\Delta\gamma$ for the forward or $\gamma_k = 2\gamma_{\max} - k\Delta\gamma$ for the reverse part of the cycle. This process is repeated for up to $n = 10^6$ cycles. Note that the simple shear applied here is uniform, and we employ Lees-Edwards periodic boundary conditions. In this method, we do not include the effects from system boundaries and nonuniform strain. However, we believe that a systematic approach where we first understand particle-scale reversibility in response to an idealized strain deformation (and then consider the response to nonuniform shear strain and wall effects) will lead to the most insight. We also note that idealized uniform simple shear strain can indeed be implemented in experiments; for example, in (i) high Peclet number, neutrally buoyant charged colloids placed in an oscillating electric field or field gradient [12,13]; (ii) disks resting on an elastic membrane that is subjected to oscillating strain; and (iii) disks resting on slats or sliders that can be moved independently [11].

We measure the single-cycle mean-square displacement (at step $k = 0$),

$$\Delta r_1^2(n) = \left(N\sigma_s^2\right)^{-1} \sum_i \left[\left(X^i_{n,0} - X^i_{n+1,0}\right)^2 + \left(Y^i_{n,0} - Y^i_{n+1,0}\right)^2 + \left(Z^i_{n,0} - Z^i_{n+1,0}\right)^2\right], \tag{3}$$

and arc length,

$$L^2(n) = \left(N\sigma_s^2\right)^{-1} \sum_i \left\{ \sum_k \left[\left(X^i_{n,k+1} - X^i_{n,k}\right)^2 + \left(Y^i_{n,k+1} - Y^i_{n,k}\right)^2 + \left(Z^i_{n,k+1} - Z^i_{n,k}\right)^2\right]^{1/2} \right\}^2, \tag{4}$$

versus n, where $X^i_{n,k} = x^i_{n,k} - \gamma_k y_{n,k}$, $Y^i_{n,k} = y^i_{n,k}$, and $Z^i_{n,k} = z^i_{n,k}$ are the nonaffine displacements of particle i after subtracting off the affine contribution. The long-time dynamics are either reversible or irreversible depending on ϕ and $\gamma_{\max}$. We quantify the steady-state behavior by measuring $\Delta r_1^2(n)$ and $L^2(n)$ of the intracycle particle trajectories (normalized by the small particle diameter).

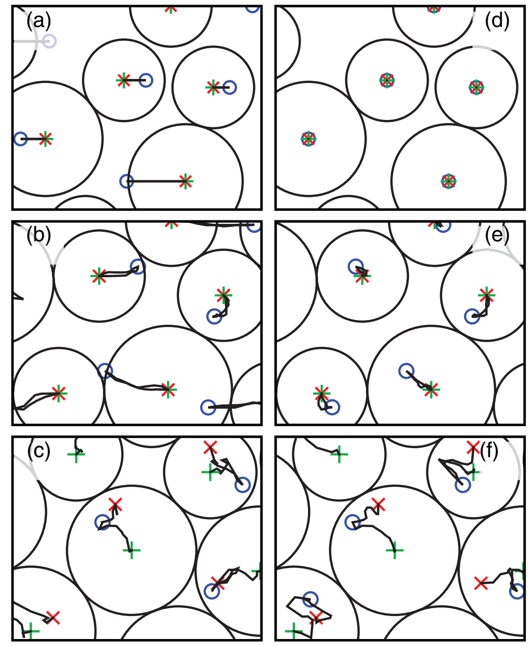

FIG. 1. (Color online) Particle tracks (solid lines) in a small window of a $N = 128$ system of bidisperse disks undergoing (a) point-reversible, (b) loop-reversible, and (c) irreversible behavior during cyclic simple shear. Panels (d), (e), and (f) show the disks' tracks in panels (a), (b), and (c), respectively, after subtracting off the affine motion. The systems in (a) and (d) correspond to $\phi = 0.64$ and $\gamma_{\max} = 0.8$, (b) and (e) to $\phi = 0.8$ and $\gamma_{\max} = 0.8$, (c) and (f) to $\phi = 0.82$ and $\gamma_{\max} = 0.8$. Pluses, circles, and crosses mark the beginning, middle, and end of the particle tracks, and particle outlines correspond to the beginning of the cycle.

We define the three classes of dynamics as follows. Particles in *point-reversible* systems organize to avoid collisions. When no collisions take place, $L(n) = \Delta r_1(n) = 0$, or more aptly, they fall below small numerical thresholds, e.g., $\Delta r_1(n) < \tau_r = 5 \times 10^{-4}$ and $L(n) < \tau_L = 10^{-8}$. The values of τ_r and τ_L do not qualitatively affect our results as long as they are sufficiently small (cf. Appendix C). Particle motions for point-reversible systems are affine and in the direction of the imposed affine shear [Fig. 1(a)]. Thus, the nonaffine tracks of each particle are zero [Fig. 1(d)]. In *loop-reversible* systems, particle collisions occur frequently, but the system self-organizes so that particles return to the same positions as at the start of each cycle. Since collisions between particles occur, $L(n) > 0$, but $\Delta r_1(n) = 0$ (i.e., below τ_r). [See Figs. 1(b) and 1(e).] Individual particle trajectories form closed loops in configuration space. We focus on period one loop-reversible systems, but multiperiod dynamics are also found. Particles in systems undergoing *irreversible* dynamics do not return to their original positions at the beginning of each cycle [Figs. 1(c) and 1(f)]. Irreversible systems have nonzero $\Delta r_1(n)$ and $L(n)$ [i.e., $L(n) > \tau_L$ and $\Delta r_1(n) > \tau_r$]. Systems can be "transient" irreversible in time and evolve into point- or loop-reversible systems or steady-state irreversible and remain irreversible in the large-cycle limit with nonzero self-diffusion.

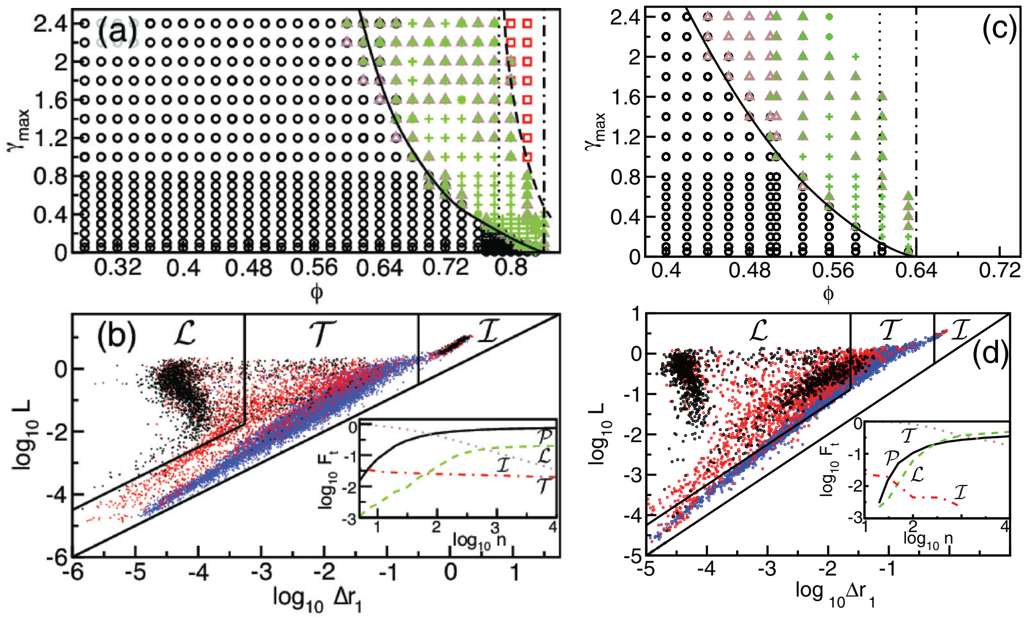

FIG. 2. (Color online) (a) "Dynamical phase diagram" for $N = 128$ bidisperse disks in 2D after $n = 10^4$ cycles showing point-reversible (circles), period-one (pluses), or multiperiod (crosses) loop-reversible, and transient (triangles) or steady-state (squares) irreversible dynamics versus $\gamma_{\max}$ and ϕ for 16 independent initial conditions. The solid and dashed lines indicate $\phi_L(\gamma_{\max})$ and $\phi_I(\gamma_{\max})$, the boundaries between point- and loop-reversible dynamics and between loop-reversible and irreversible dynamics, respectively. The vertical dotted and dot-dashed lines define $\phi_R = \pi/4 \simeq 0.785$ and $\phi_J \approx 0.84$. (b) Arc-length L vs. intracycle mean-square displacement Δr_1 after $n = 10$ (blue), 3×10^2 (red), and 10^4 (black) cycles. The regions labeled $\mathcal{L}$, $\mathcal{T}$, and $\mathcal{I}$ define loop-reversible, transient irreversible, and steady-state irreversible dynamics, respectively. The point-reversible ($\mathcal{P}$) region extends from $L = \Delta r_1 = 10^{-6}$ to 10^{-16} but is not shown. The dashed boundaries indicate $\Delta r_1 = \tau_r$, $\Delta r_1 = 0.3$, $L = \tau_L$, $L = 30\Delta r_1$, and $L = \Delta r_1$ discussed in the main text. The inset shows the fraction F_t of systems in (a) categorized as point-reversible (solid), loop-reversible (dashed), transient irreversible (dotted), and irreversible (dot-dashed) dynamics versus n. Panels (c) and (d) show the same data as (a) and (b) but for 3D systems.

We also studied the structural properties of the systems as a function of ϕ and $\gamma_{\max}$. We measured the global (ψ_6^g) and local (ψ_6^l) bond-orientational order parameters [14] and the layering order parameters [15] in the directions perpendicular ($l_\perp$) and parallel ($l_{||}$) to the applied strain:

$$l_{||} = \frac{1}{N}\sum_{i=1}^{N}\frac{1}{N_n^i}\sum_{j=1}^{N_n^i}\cos(2\pi x_{ij}/\sigma_{ij}) \tag{5}$$

$$l_\perp = \frac{1}{N}\sum_{i=1}^{N}\frac{1}{N_n^i}\sum_{j=1}^{N_n^i}\cos(2\pi y_{ij}/\sigma_{ij}), \tag{6}$$

where N_n^i is the number of neighbors of particle i (with $r_{ij} \leqslant 1.5\sigma_{ij}$).

III. RESULTS

A. Phase diagrams for 2D and 3D

The steady-state "dynamical phase diagram" in Fig. 2(a) for cyclically sheared athermal disks shows point- and loop-reversible, as well as irreversible regimes versus ϕ and $\gamma_{\max}$ for systems in 2D. Point-reversible systems occur at low ϕ and $\gamma_{\max}$, whereas irreversible systems occur for $\phi \gtrsim \phi_J$ [16,17]. At intermediate packing fractions between contact percolation [10] and the onset of jamming, e.g., $0.6 \lesssim \phi \lesssim 0.84$ in 2D, loop-reversible systems are found. The boundary between point- and loop-reversible systems is $\gamma_{\max} \sim A(\phi)(\phi_J - \phi)^\lambda \Theta(\phi_J - \phi)$, where $A(\phi)$ depends weakly on ϕ and $\lambda \sim 1.2 \pm 0.1$ for $\phi \to \phi_J$ and 2.2 ± 0.2 for $\phi \ll \phi_J$. Over a finite number of cycles [i.e., $n < 10^4$ in Fig. 2(b)], transient irreversible dynamics can occur, but these systems become point-reversible, loop-reversible, or steady-state irreversible as $n \to \infty$. Point-reversible systems tend to form ordered, size-segregated layers (cf. Sec. III C), in which particles cannot collide during simple shear. Further, the loop-reversible to irreversible transition in steady-state $\phi_I(\gamma_{\max})$ is bounded in the large-$\gamma_{\max}$ limit by the highest packing fraction $\phi_R = \pi/4 \simeq 0.785$ at which systems in 2D can form size-segregated layers in the $N \to \infty$ limit.

In Fig. 2(b), scatter plots of $L(n)$ versus $\Delta r_1(n)$ illustrate the evolution of the dynamics with increasing n. The points form several well-defined clusters: point-reversible ($\mathcal{P}$) with $L < \tau_L$ and $\Delta r_1 < \tau_r$, loop-reversible ($\mathcal{L}$) with nonzero L ($L > \tau_L$) and $\Delta r_1 < \tau_r$, and irreversible ($\mathcal{I}$) with nonzero L ($L > \tau_L$) and Δr_1 ($\Delta r_1 > \tau_r$). The $\mathcal{P}$, $\mathcal{L}$, and $\mathcal{I}$ clusters are separated by more than 3 orders of magnitude in Δr_1 or L. For region L, we also mandate $L > 30\Delta r_1$ since systems with $L < 30\Delta r_1$ typically relax to point-reversible states. We also enforce $\Delta r_1 > 0.3$ to define region $\mathcal{I}$ since systems with $\Delta r_1 < 0.3$ typically relax to point- or loop-reversible states. Systems that do not fall within regions $\mathcal{P}$, $\mathcal{L}$, and $\mathcal{I}$ are categorized as transient irreversible ($\mathcal{T}$). As n increases, the fraction F_t of systems in the transient regime vanishes as a power-law

$n^{-\alpha}$ ($\alpha \approx 0.56 \pm 0.01$), while the fraction of point-reversible, loop-reversible, and steady-state irreversible systems saturates near 10^4 cycles [inset to Fig. 2(b)].

Three-dimensional systems exhibit qualitatively similar behavior. Figure 2(c) shows the dynamical phase diagram for 3D bidisperse systems (50-50 mixtures with size ratio $d = 1.4$) for $N = 128$ after $n = 10^4$ cycles. We find a point- to loop-reversible transition when the packing fraction $\phi > \phi_L(\gamma_{\max})$, where $\phi_L(\gamma_{\max})$ approaches random close packing $\phi_J \approx 0.65$ [18] (for bidisperse mixtures) in the limit $\gamma_{\max} \to 0$. In Fig. 2(d), we show the evolution of dynamics with increasing n, which is also similar to that illustrated in Fig. 2(b). Thus, we conclude that the response to cyclic shear is not sensitive to spatial dimension for these bidisperse mixtures, and for the remainder of this paper we focus on 2D systems.

B. Approach to steady-state dynamics

Next we characterize the dynamics as the systems approach steady-state point- and loop-reversible states [Fig. 3(a)]. We find that the single-cycle mean-square displacement can be described by a function that interpolates between power-law and exponential decays at short and long times, respectively:

$$\Delta r_1^f(n) = f_+(n)(n/n_c)^{-\alpha} + f_-(n)e^{-\beta(n-n_c)}, \tag{7}$$

where $f_\pm(n) = (1 + e^{\pm\overline{\gamma}(n-n_c)})^{-1}$, $\overline{\gamma} \sim 1$, n_c is the cycle number at which the decay changes from power-law to exponential behavior, α is a power-law scaling exponent, and β characterizes the exponential decay.

In Fig. 3(b), we plot the best fit $\Delta r_1^f(n)$ versus $\Delta r_1(n)$ at each $\gamma_{\max}$ and ϕ for systems in Fig. 2 that evolve to point-reversible states. The scaling function in Eq. (7) collapses more than 60% of point-reversible systems with deviations $\Delta = \langle(\log_{10}\Delta r_1^f(n) - \log_{10}\Delta r_1(n))^2\rangle < 0.18$. The top and bottom insets in Fig. 3(b) show the power-law scaling and exponential decay of $\Delta r_1(n)$ separately. We find similar scaling for the approach to loop-reversible states. However, the exponential decay for loop-reversible systems is difficult to differentiate from numerical error because the long-time dynamics occurs at larger n_c and smaller Δr_1 than that for point-reversible systems. In Fig. 3(c), we show the power-law decay for all systems that evolve to loop-reversible dynamical states. In the inset, we also show several systems for which we captured the long-time exponential decay.

In Fig. 4(a), we show the power-law scaling exponent α for systems that evolve to point- and loop-reversible states versus ϕ and $\gamma_{\max}$. We find that $\alpha \lesssim 1$ for all loop-reversible systems and point-reversible systems near the crossover from point- to loop-reversible behavior, which suggests that the origin of the slow dynamics is related to contact or "collision" percolation. In contrast, $\alpha > 1$ for point-reversible systems at low ϕ and $\gamma_{\max}$. In Fig. 4(b), we find that n_c increases with ϕ and $\gamma_{\max}$ and appears to be diverging as the system approaches the transition from point- to loop-reversibility.

We tested the stability of the point- and loop-reversible states by perturbing all particles at strain $\gamma = 0$ by an amplitude δ in random directions. We then performed cyclic simple shear on the perturbed system and measured the deviation, $\Delta_r = \sqrt{(N\sigma_s^2)^{-1}\sum_i |\vec{r}^{\,i}_{n,0} - \vec{r}^{\,i,p}_{n,0}|^2}$, where $\vec{r}^{\,i,p}_{n,0}$ are the coordinates of the perturbed system after t cycles required to reach steady state at each ϕ and $\gamma_{\max}$. We find that $\Delta_r \sim \delta$ for point-reversible systems. Thus, point-reversible states are only marginally stable with interconnected regions of configuration space. In contrast, loop-reversible systems are stable (with vanishing $\Delta_r < \tau_r$) for perturbations $\delta < \delta_c \simeq 10^{-1}$, where δ_c is relatively insensitive to ϕ for $\gamma_{\max} \lesssim 1$. Further details are given in Appendix B.

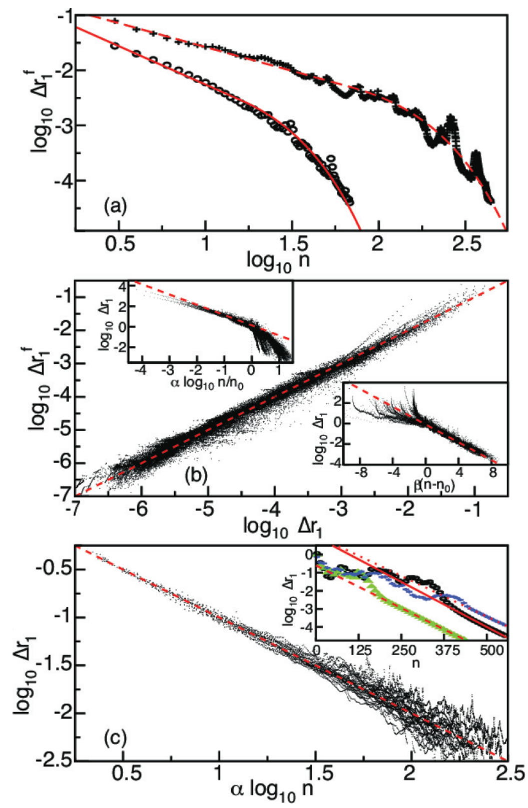

FIG. 3. (Color online) (a) Single-cycle mean-square displacement Δr_1 versus n for a point-reversible system at $\phi = 0.64$ and $\gamma_{\max} = 0.5$ (circles) and loop-reversible system at $\phi = 0.8$ and $\gamma_{\max} = 0.5$ (pluses) with best fits to Δr_1^f [Eq. (7)] indicated by solid and dashed lines. (b) Comparison of $\Delta r_1(n)$ (averaged over 16 initial conditions for each $\gamma_{\max}$ and ϕ) to $\Delta r_1^f(n)$ (black dots) for point-reversible systems in Fig. 2 with $\Delta < 0.18$. $\Delta r_1^f(n) = \Delta r_1(n)$ is indicated by the dashed line. The top left inset shows $\log_{10}\Delta r_1(n)$ versus $\alpha\log_{10} n/n_c$ (black dots). The dashed line indicates $\Delta r_1(n) = (n/n_c)^{-\alpha}$. The bottom right inset shows $\log_{10}\Delta r_1(n)$ versus $\beta(n-n_c)$ (black dots). $\Delta r_1(n) = e^{-\beta(n-n_c)}$ is indicated by the dashed line. (c) $\log_{10}\Delta r_1(n)$ versus $\alpha\log_{10} n$ (black dots) for systems in Fig. 2 that evolve to loop-reversible states with $\Delta < 0.04$. $\Delta r_1(n) = n^{-\alpha}$ is indicated by the dashed line. The inset shows Δr_1 versus n for three independent initial conditions at $\phi = 0.76$ and $\gamma_{\max} = 0.8$. Exponential fits to the large-n regime are shown as solid, dashed, and dotted lines with slopes $\beta = 0.029$, 0.026, and 0.016, respectively.

C. Structural order

Our simulations employ initial conditions wherein particles are placed randomly in the simulation cell, i.e., large and small particles are fully "mixed." For intermediate ϕ well below jamming, as the number of cycles n increases, large and small particles can phase-separate. Experiments have shown [1]

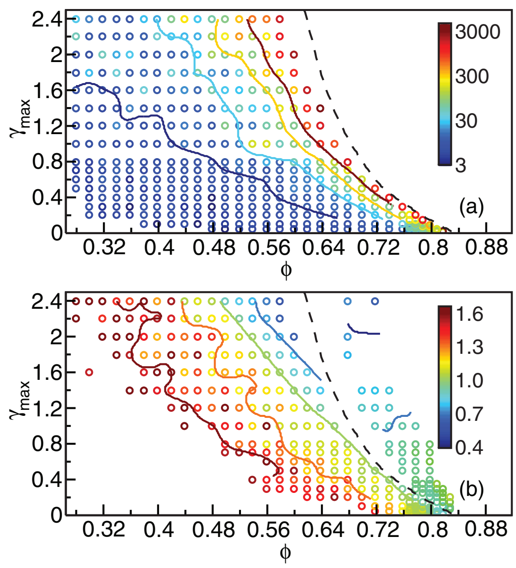

FIG. 4. (Color online) (a) Contour plot of the power-law exponent α [Eq. (7)] versus ϕ and $\gamma_{\max}$ for systems that evolve to either point- (circles) or loop-reversible (crosses) states. (b) Contour plot of n_c [Eq. (7)] that controls the crossover from power-law to exponential decay versus ϕ and $\gamma_{\max}$ for point-reversible systems in (a).

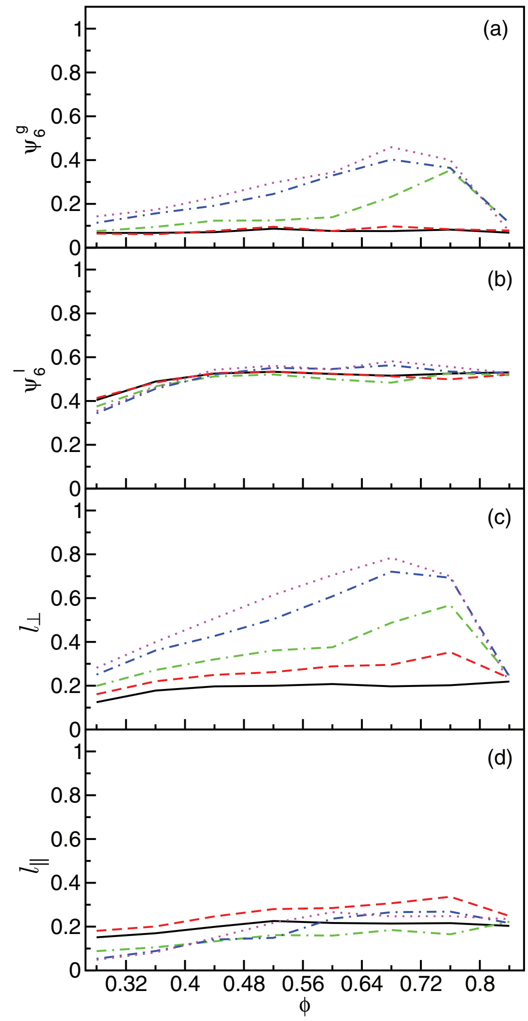

FIG. 5. (Color online) (a) Global ψ_6^g and (b) local ψ_6^l bond-orientational order parameters and layer order parameters (c) $l_\perp$ and (d) $l_{||}$ for $N = 128$ systems after $n = 10^4$ cycles with no applied shear (solid black) and maximum simple shear strain $\gamma_{\max} = 0.4$ (red dashed), 0.8 (green dash-dash-dotted), 1.6 (blue dash-dotted), and 2.4 (purple dotted) as a function of packing fraction ϕ.

that granular materials tend to crystallization upon shearing, which could cause reversibility, i.e., particles do not touch or collide, but rather occupy the sites of a (macroscopically phase-separated) hexagonal lattice. If this is true, there should be another transition from irreversible to reversible, when crystallization appears at any density $\phi < \phi_{\rm xtal}$, where the close-packed crystalline density $\phi_{\rm xstal} \simeq 0.91$ (2D) and $\simeq 0.74$ (3D).

Alternatively, systems can microphase-separate into "lanes" [13] of large and small particles with positional ordering along the y but not the x or z directions, with maximum packing fraction $\phi_R = \pi/4$ (2D) and $\pi/6$ (3D). It is important to examine which of these two possibilities occur in our simulations. We do so using the order parameters ψ_6^g, ψ_6^l, $l_{||}$, and $l_\perp$ [Eqs. (5)–(8)]. Figure 5 shows results for 2D systems. We find that layering (not hexagonal ordering) becomes stronger with increasing ϕ and $\gamma_{\max}$. This is evident in both $l_\perp$ and ψ_6^g, which approach their limiting values, $l_\perp = 1$ and $\psi_6^g = 0.56$, for a fully layered system with no correlations between successive layers.

IV. DISCUSSION

Many particulate systems possess static frictional interactions in addition to the purely repulsive contact interactions included in the present computational model and undergo fluctuations (either thermal or mechanical). However, the individual contributions to reversibility from each of these effects are not known, and it is extremely difficult to disentangle the effects of steric interactions, friction, and fluctuations when all are included at once. Here we investigated the role of purely repulsive interactions (as well as dissipation) by mapping out in what parameter regimes in the packing fraction and shear amplitude plane particulate systems are reversible versus irreversible. Prior to our studies, we argue that many would have thought that athermal particulate systems are always irreversible, without point and loop reversible states. In particular, one might argue that at very low densities, any fluctuations or perturbations (not necessarily thermal fluctuations) eliminate reversibility, so that the low-density states investigated here should be irreversible rather than reversible. Our results for point- and loop-reversibility show the contrary.

The advantage of the reductionist approach employed here is that we better understand the role of purely repulsive contact interactions, and are now in a position to add fluctuations and frictional interactions to investigate their effects separately. Note that this modeling approach has been applied successfully during the past decade to understand jamming transitions in particulate systems, first in systems of frictionless spherical particles at zero temperature [19], in systems with static friction [20], with thermal fluctuations [21], and in systems composed of nonspherical particles [22]. In addition, this approach can be applied in experiments that examine athermal particulate media—friction can be reduced using hydrogel [23] or teflon [24] particles and affine shear can be applied in 2D systems without large fluctuations using the experimental setup described in Ref. [11]. We believe that the results presented here should apply to most quasistatically shear-driven granular and athermal systems [25,26].

V. CONCLUSIONS

We studied the extent to which particle-scale motion is reversible in athermal systems undergoing cyclic loading. We identified two types of reversible behavior. For point-reversible states, particles do not collide and trivially retrace their paths. For loop-reversible states, all particles undergo multiple collisions, yet all particles return to where they were at the beginning of each cycle. We find that loop-reversible states are stable and occur over a range of packing fractions from contact percolation [10] to jamming onset, and thus our results emphasize that complex spatiotemporal dynamics occur well below ϕ_J. Loop-reversibility enables reliable preparation of athermal systems with dynamically tunable structural and rheological properties over a broad range of packing fractions, using strain as the control parameter. For example, the fact that particles in loop-reversible states undergo collisions without diffusion can be exploited in applications that range from catalysts to pharmaceutical powders.

In future studies, we will investigate the role of static friction on reversibility in granular systems, which we expect will lead to only quantitative changes in the dynamical phase diagram, and study systems above jamming to determine the connection between the breakdown of elastic behavior and the transition from reversible to irreversible motion. We suggest that new experiments be performed to probe the behavior of athermal particulate media as a function of packing fraction and strain amplitude to investigate the proposed phase diagram. We encourage studies: (i) examining a range of particle interactions from frictionless to highly frictional, (ii) employing different methods for applying the strain (e.g., pure and simple shear and extensional deformations), and (iii) investigating the effects of fluctuations both thermal and mechanical. The point and loop reversible regimes can be mapped out in the phase diagram using 3D particle tracking methods such as confocal microscopy [27] and refractive index matched scanning [28].

ACKNOWLEDGMENTS

Support from NSF Grants No. NSF MRSEC DMR-1119826 (C.S.), No. DMR-1006537 (R.H.), No. CBET-0968013 (M.S.), and No. CBET-0967262 (C.O.) is gratefully acknowledged.

APPENDIX A: SYSTEM-SIZE DEPENDENCE

We find only weak finite-size effects in systems undergoing cyclic simple shear. In Fig. 6, we compare the dynamical phase diagrams for 2D bidisperse systems with $N = 64$ and 256. For both system sizes, we find a transition from point- to loop-reversible dynamics for $\phi > \phi_L(\gamma_{\max})$ and then from loop-reversible to irreversible dynamics for $\phi > \phi_I(\gamma_{\max})$, though

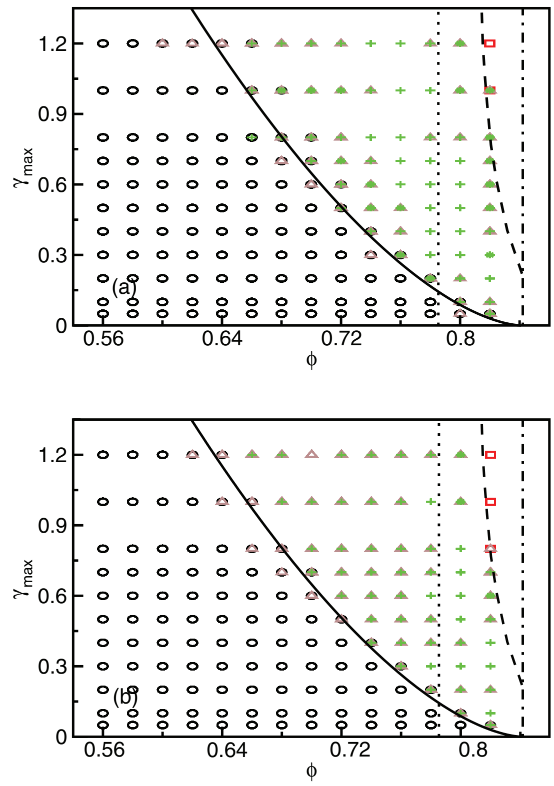

FIG. 6. (Color online) Dynamical phase diagram for (a) $N = 64$ and (b) 256 bidisperse disks subjected to cyclic simple shear after $n = 10^3$ cycles, showing point-reversible (circles), period-one (pluses), or multiperiod (crosses) loop-reversible, and transient (triangles) or steady-state (squares) irreversible dynamics versus $\gamma_{\max}$ and ϕ (for 16 independent initial conditions). The solid and dashed lines indicate $\phi_L(\gamma_{\max})$ and $\phi_I(\gamma_{\max})$, the boundaries between point- and loop-reversible dynamics and between loop-reversible and irreversible dynamics, respectively. The vertical dotted and dot-dashed lines define $\phi_R = 0.785$ and $\phi_J \approx 0.84$, respectively.

systems with $N = 64$ display more coexistence of point- and loop-reversible dynamical states near $\phi_L(\gamma_{\max})$ than systems with $N = 256$.

The best fit for $\phi_L(\gamma_{\max})$ obeys

$$\phi_L(\gamma_{\max}) \propto (\phi - \phi_J)^{\alpha}\Theta(\phi_J - \phi), \tag{A1}$$

where $\alpha \simeq 1.6 \pm 0.4$ for both $N = 64$ and 256. Note that the power-law exponent $\alpha \simeq 1.6$ for systems with $N = 64$ and 256 at $n = 10^3$ cycles is larger than that found for $N = 128$ systems at $n = 10^4$ cycles. We find that the large-n limit for the power-law exponent α is closer to 1 than 2. Also, systems with $N = 256$ particles possess a smaller region in the L and Δr_1 plane for which all trials generate loops at $n = 10^3$ cycles. This signals the growth in the relaxation time (or number of cycles) n_c with N after which systems reach steady-state loop-reversible states.

We find only small differences in the single-cycle mean-square displacement Δr_1, arc-length L, and packing fraction $\phi_L(\gamma_{\max})$ for system sizes with $N \geqslant 64$. In Fig. 7(a), we show Δr_1 versus L for $N = 64$ and 256 after 10^3 cycles. For both system sizes, the clusters of points representing point- and loop-reversible as well as steady-state irreversible dynamics

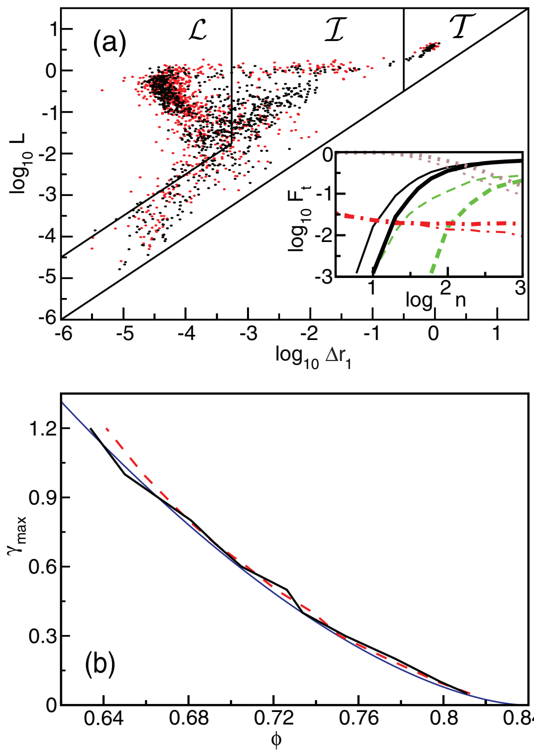

FIG. 7. (Color online) The arc length L versus the single-cycle mean-square displacement Δr_1 after $n = 10^3$ cycles for 2D systems with $N = 64$ (red points) and 256 (black points). The regions labeled $\mathcal{L}$, $\mathcal{T}$, and $\mathcal{I}$ define loop-reversible, transient-irreversible, and steady-state irreversible dynamics, respectively, using the same boundary lines as those in Fig. 2(b). In the inset, we show the fraction of systems that are point-reversible (solid), loop-reversible (dashed), transient (dotted), and irreversible (dot-dashed) as a function of cycle number n for $N = 64$ (thin) and 256 (thick). (b) The maximum shear strain amplitude $\gamma_{\max}$ versus the packing fraction $\phi_L(\gamma_{\max})$, above which the system transitions from point- to loop-reversible dynamics after $n = 10^3$ cycles for $N = 64$ (dashed) and 256 (solid). The best fit to Eq. (A1) is shown as a thin dotted line.

are in the same regions of the Δr_1 and L plane. However, there are more points in the "transient" region for $N = 256$.

In the inset to Fig. 7(a), we show the fraction of systems in the parameter space shown in Fig. 6 that are point reversible, loop reversible, transient, and irreversible as a function of cycle number n. We find qualitatively similar behavior for $N = 64$ and 256. Both show an increasing fraction of point- and loop-reversible systems that are beginning to reach their large-n plateau values at $n = 10^3$ cycles and a continuously decreasing fraction of transient states. Notice that the fraction of point- and loop-reversible systems decays to the large-n limit more slowly for $N = 256$ than for $N = 64$. Finally, in Fig. 7(b), we show explicitly that $\phi_L(\gamma_{\max})$ does not depend on system size for $N \geqslant 64$ for $\gamma_{\max} < 1$, and $\phi_L \to \phi_J \approx 0.84$ in the limit $\gamma_{\max} \to 0$.

APPENDIX B: LOOP STABILITY

To test the stability of steady-state point- and loop-reversible systems in 2D, we perturb the x- and y-coordinates

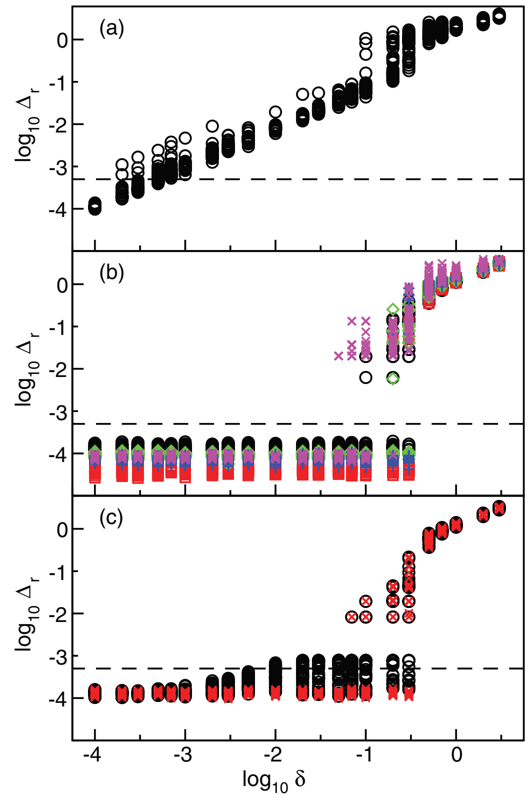

FIG. 8. (Color online) (a) Deviation Δ_r between the particle coordinates of the original and perturbed trajectories after $n = 10^3$ cycles following the perturbation as a function of the perturbation amplitude δ for a point-reversible system at $\phi = 0.62$ and $\gamma_{\max} = 2.0$. Data is shown for 40 independent random perturbations at each δ. (b) Δ_r versus δ for stable loop-reversible systems at $\phi = 0.8$ and $\gamma_{\max} = 0.2$ (circles), 0.83 and 0.2 (squares), 0.74 and 0.8 (diamonds), 0.8 and 0.8 (pluses), and 0.74 and 1.4 (crosses). (c) Δ_r versus δ for a loop-reversible system with 1 dynamical floater at $\phi = 0.83$ and $\gamma_{\max} = 0.1$ (circles), and with the the dynamical floater removed from the calculation of Δ_r (crosses).

of all particles at cycle n_0 and strain $\gamma = 0$,

$$x_{0,0}^{i,p} = x_{n_0,0}^{i} + \sigma_s \delta_x^i, \tag{B1}$$

$$y_{0,0}^{i,p} = y_{n_0,0}^{i} + \sigma_s \delta_y^i, \tag{B2}$$

where σ_s is the small particle diameter, δ_x^i and δ_y^i are chosen from Gaussian distributions centered at zero with standard deviation $\delta/\sqrt{2}$, and the average perturbation amplitude is $\delta = \sqrt{(\sum_i (\delta_x^i)^2 + (\delta_y^i)^2)/N}$. We then perform cyclic simple shear on the perturbed system and measure the deviation between the perturbed and unperturbed particle trajectories, $\Delta_r = \sqrt{(N\sigma_s^2)^{-1}\sum_i |\vec{r}_{n,0}^{\,i} - \vec{r}_{n,0}^{\,i,p}|^2}$, where $\vec{r}_{n,0}^{\,i,p}$ are the coordinates of the perturbed system after t cycles required to reach steady-state at each ϕ and $\gamma_{\max}$.

In Fig. 8(a), we show the deviation Δ_r between the unperturbed and perturbed particle positions at $\gamma = 0$ for a system undergoing point-reversible dynamics at $\phi = 0.62$ and $\gamma_{\max} = 2.0$. We find that Δ_r scales with the perturbation amplitude over a wide range of δ, which indicates that point-reversible systems are only marginally stable.

In Fig. 8(b), we show the deviation Δ_r between the unperturbed and perturbed particle positions at $\gamma = 0$ for loop-reversible systems in the range $0.74 < \phi < 0.83$ and $0.1 < \gamma_{\max} < 1.4$. We find that these systems are stable because there is a finite range of perturbation amplitudes $0 < \delta < \delta^*$ over which Δ_r is below numerical precision (i.e., $\Delta_r < \tau_r$).

Loop-reversible systems near $\phi_L(\gamma_{\max})$ can possess "dynamical floaters," which are particles that do not incur any collisions during a shear cycle, and thus their motion is affine. In point-reversible systems, all particles are by definition "dynamical floaters." The loop-reversible systems in Fig. 8(b) have no dynamical floaters. In Fig. 8(c), we show Δ_r as a function of δ for loop-reversible systems with a single dynamical floater. If we include the dynamical floater in the calculation of the deviation in the positions, Δ_r begins to increase for $\delta > 10^{-3}$. When the dynamical floater is removed from the calculation of Δ_r, we show that the loop-reversible state is stable for $\delta < \delta_c \approx 10^{-1}$. Determining the stability of loop-reversible systems is difficult for $\gamma_{\max} > 1$ because δ_c decreases with increasing $\gamma_{\max}$.

APPENDIX C: EFFECTS OF NUMERICAL PRECISION

The error ΔL in the calculation of the arc length L for loop-reversible systems has contributions from the size of the shear strain step $\Delta\gamma$ and the energy minimization tolerance $V_{\rm tol}$:

$$\Delta L \sim k_1 \Delta\gamma + k_2\sqrt{V_{\rm tol}}, \tag{C1}$$

where k_1 and k_2 are order-one constants. Here we explore the sensitivity of our results to the size of the shear strain step and energy minimization tolerance.

1. Shear strain step size

We apply simple shear strain successively in increments of $\Delta\gamma$,

$$x^i_{n,k+1} = x^i_{n,k} + \Delta\gamma y^i_{n,k}, \tag{C2}$$

where $\Delta\gamma \ll 1$. For the results presented in the main text, we employ $\Delta\gamma = 10^{-3}$, but here we show that the results for the arc length and single-cycle mean-square displacement are not sensitive to the size of the shear strain step for $\Delta\gamma < 10^{-2}$.

In Fig. 9(a), we show the single-cycle arc-length $\langle L\rangle$ (averaged over 16 independent trajectories) as a function of the cycle number n for shear strain amplitude $\gamma_{\max} = 0.3$, packing fraction from $\phi = 0.56$ to 0.83, and shear strain step size from $\Delta\gamma = 10^{-4}$ to 10^{-2}. For all ϕ studied, $\langle L\rangle$ does not depend sensitively on $\Delta\gamma$. Note that in Fig. 9 we chose a small value $V_{\rm tol} = 10^{-16}$ for the energy minimization tolerance, so that $\Delta\gamma$ determines the accuracy of the calculation of $\langle L\rangle$.

2. Energy minimization tolerance

After each strain increment, we minimize the total potential energy of the system V until one of the following conditions is satisfied:

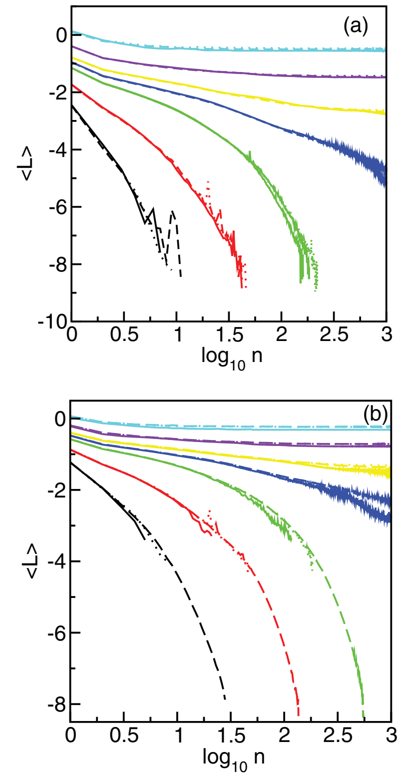

FIG. 9. (Color online) Arc-length $\langle L\rangle$ averaged over 16 independent trajectories versus cycle number n for systems of size $N = 128$ at maximum shear strain amplitude $\gamma_{\max} = 0.3$, packing fraction $\phi = 0.32$ (black), 0.56 (red), 0.72 (green), 0.76 (blue), 0.78 (yellow), 0.81 (purple), and 0.83 (cyan). (a) Effect of shear strain increment $\Delta\gamma = 10^{-2}$ (solid), 10^{-3} (dotted), and 10^{-4} (dashed) for energy minimization tolerance $V_{\rm tol} = 10^{-16}$. (b) Effect of energy minimization tolerance $V_{\rm tol} = 10^{-16}$ (solid), 10^{-8} (dotted), and 10^{-6} (dashed) for shear strain increment $\Delta\gamma = 10^{-3}$.

$$V_l/(N\epsilon) < V_{\rm tol}, \tag{C3}$$

$$|V_l - V_{l-1}|/V_l < V_{\rm tol}, \tag{C4}$$

where V_l is the potential energy after the lth minimization step and ϵ is the unit of energy. The first condition corresponds to an "unjammed" configuration with approximately zero potential energy, and the second corresponds to a "jammed" configuration with finite potential energy and pressure. Figure 9(b), which plots the arc length $\langle L\rangle$ versus n for the energy minimization tolerance from $V_{\rm tol} = 10^{-16}$ to 10^{-6}, shows that the arc length does not depend sensitively on $V_{\rm tol}$ provided that it is sufficiently small. Note that $\langle L\rangle \sim \sqrt{V_{\rm tol}}$ for point-reversible systems (i.e., systems with $0.56 < \phi < 0.72$ in Fig. 9). For loop-reversible systems (i.e., systems with $0.81 < \phi < 0.83$ in Fig. 9), the large-n value of the arc length is independent of $V_{\rm tol}$, but depends on ϕ and $\gamma_{\max}$.

[1] M. Nicolas, P. Duru, and O. Pouliquen, Eur. Phys. J. E **3**, 309 (2000).

[2] E. R. Nowak, J. B. Knight, E. Ben-Naim, H. M. Jaeger, and S. R. Nagel, Phys. Rev. E **57**, 1971 (1998).

[3] M. Lundberg, K. Krishan, N. Xu, C. S. O'Hern, and M. Dennin, Phys. Rev. E **77**, 041505 (2008).
[4] D. J. Pine, J. P. Gollub, J. F. Brady, and A. M. Leshansky, Nature **438**, 997 (2005).
[5] L. Corte, P. M. Chaikin, J. P. Gollub, and D. J. Pine, Nature Physics **4**, 420 (2008).
[6] I. Regev, T. Lookman, and C. Reichhardt, http://xxx.lanl.gov/pdf/1301.7479.pdf.
[7] S. Slotterback, M. Mailman, K. Ronaszegi, M. van Hecke, M. Girvan, and W. Losert, Phys. Rev. E **85**, 021309 (2012).
[8] M. P. Allen and D. J. Tildesley, *Computer Simulation of Liquids* (Oxford University Press, New York, 1987).
[9] G.-J. Gao, J. Blawzdziewicz, and C. S. O'Hern, Phys. Rev. E **80**, 061303 (2009).
[10] T. Shen, C. S. O'Hern, and M. D. Shattuck, Phys. Rev. E **85**, 011308 (2012).
[11] J. Ren, J. A. Dijksman, and R. P. Behringer, Phys. Rev. Lett. **110**, 018302 (2013).
[12] T. Vissers, A. Wysocki, M. Rex, H. Löwen, C. P. Royall, A. Imhof, and A. van Blaaderen, Soft Matter **7**, 2352 (2011).
[13] J. Dzubiella, G. P. Hoffmann, and H. Löwen, Phys. Rev. E **65**, 021402 (2002).
[14] P. J. Steinhardt, D. R. Nelson, and M. Ronchetti, Phys. Rev. B **28**, 784 (1983).
[15] Y. Takanishi, A. Ikeda, H. Takezoe, and A. Fukuda, Phys. Rev. E **51**, 400 (1995).
[16] D. J. Lacks, Molec. Sim. **30**, 831 (2004).
[17] I. K. Ono, C. S. O'Hern, D. J. Durian, S. A. Langer, A. J. Liu, and S. R. Nagel, Phys. Rev. Lett. **89**, 095703 (2002).
[18] N. Xu and C. S. O'Hern, Phys. Rev. Lett. **94**, 055701 (2005).
[19] C. S. O'Hern, L. E. Silbert, A. J. Liu, and S. R. Nagel, Phys. Rev. E **68**, 011306 (2003).
[20] S. Papanikolaou, C. S. O'Hern, and M. D. Shattuck, Phys. Rev. Lett. **110**, 198002 (2013).
[21] C. F. Schreck, T. Bertrand, C. S. O'Hern, and M. D. Shattuck, Phys. Rev. Lett. **107**, 078301 (2011).
[22] M. Mailman, C. F. Schreck, C. S. O'Hern, and B. Chakraborty, Phys. Rev. Lett. **102**, 255501 (2009).
[23] K. Chen *et al.*, Phys. Rev. Lett. **105**, 025501 (2010).
[24] C. Daraio, V. F. Nesterenko, E. B. Herbold, and S. Jin, Phys. Rev. E **72**, 016603 (2005).
[25] M. M. Bandi, M. K. Rivera, F. Krzakala, and R. E. Ecke, Phys. Rev. E **87**, 042205 (2013).
[26] D. Bi, J. Zhang, B. Chakraborty, and R. P. Behringer, Nature **480**, 355 (2011).
[27] X. Cheng, X. Xu, S. A. Rice, A. R. Dinner, and I. Cohen, Proc. Natl. Acad. Sci. USA **109**, 63 (2012).
[28] J. A. Dijksman, F. Rietz, K. A. Lorincz, M. van Hecke, and W. Losert, Rev. Sci. Instrum. **83**, 011301 (2012).